Fast and Selective Super-Resolution Ultrasound In Vivo With Acoustically Activated Nanodroplets

Kai Riemer, *Member, IEEE*, Matthieu Toulemonde, *Member, IEEE*, Jipeng Yan, *Member, IEEE*, Marcelo Lerendegui, *Member, IEEE*, Eleanor Stride, Peter D. Weinberg, Christopher Dunsby, and Meng-Xing Tang, *Senior Member, IEEE*

***Abstract*— Perfusion by the microcirculation is key to the development, maintenance and pathology of tissue. Its measurement with high spatiotemporal resolution is consequently valuable but remains a challenge in deep tissue. Ultrasound Localization Microscopy (ULM) provides very high spatiotemporal resolution but the use of microbubbles requires low contrast agent concentrations, a long acquisition time, and gives little control over the spatial and temporal distribution of the microbubbles. The present study is the first to demonstrate Acoustic Wave Sparsely-Activated Localization Microscopy (AWSALM) and fast-AWSALM for *in vivo* super-resolution ultrasound imaging, offering contrast on demand and vascular selectivity. Three different formulations of acoustically activatable contrast agents were used. We demonstrate their use with ultrasound mechanical indices well within recommended safety limits to enable fast on-demand sparse activation and destruction at very high agent concentrations. We produce super-localization maps of the rabbit renal vasculature with acquisition times between 5.5 s and 0.25 s, and a 4-fold improvement in spatial resolution. We present the unique selectivity of AWSALM in visualizing specific vascular branches and downstream microvasculature, and we show super-localized kidney structures in systole (0.25 s) and diastole (0.25 s) with fast-AWSALM outperforming microbubble based ULM. In conclusion, we demonstrate the feasibility of fast and selective imaging of microvascular dynamics *in vivo* with subwavelength resolution using ultrasound and acoustically activatable nanodroplet contrast agents.**

***Index Terms*— Phase-change contrast agent, low-boiling point nanodroplet, acoustic vaporization, droplet activation, microcirculation, contrast enhanced ultrasound, plane wave activation, SRUS, ULM.**

Manuscript received 22 July 2022; revised 27 September 2022 and 8 November 2022; accepted 13 November 2022. Date of publication 18 November 2022; date of current version 3 April 2023. This work was supported in part by the Engineering and Physical Sciences Research Council (EPSRC) under Grant EP/T008970/1, Grant EP/T008067/1, and Grant EP/N026942/1; in part by the EPSRC Impact Acceleration Account under Grant EP/R511547/1; in part by the National Institute for Health Research Invention for Innovation (i4i) under Grant NIHR200972; and in part by the British Heart Foundation under Grant PG/18/48/33832. *(Corresponding author: Meng-Xing Tang.)*

This work involved human subjects or animals in its research. Approval of all ethical and experimental procedures and protocols was granted by the Animal welfare and Ethical Review Body of Imperial college London under Project License No. P15180DF2.

Kai Riemer, Matthieu Toulemonde, Jipeng Yan, Marcelo Lerendegui, Peter D. Weinberg, and Meng-Xing Tang are with the Department of Bioengineering, Imperial College London, SW7 2AZ London, U.K. (e-mail: k.riemer16@imperial.ac.uk; m.toulemonde@imperial.ac.uk; j.yan19@imperial.ac.uk; m.lerendegui@imperial.ac.uk; p.weinberg@imperial.ac.uk; mengxing.tang@imperial.ac.uk).

Eleanor Stride is with the Institute of Biomedical Engineering, University of Oxford, OX3 7LD Oxford, U.K. (e-mail: eleanor.stride@eng.ox.ac.uk).

Christopher Dunsby is with the Department of Physics, Imperial College London, SW7 2AZ London, U.K. (e-mail: christopher.dunsby@imperial.ac.uk).

This article has supplementary material provided by the authors and color versions of one or more figures available at https://doi.org/10.1109/TMI.2022.3223554.

Digital Object Identifier 10.1109/TMI.2022.3223554

I. Introduction

THE microvasculature plays a critical role in the functioning of healthy tissue. Changes in its structure and dynamics are an important diagnostic indicator in many diseases. For example, angiogenesis regulates the rate of tumor growth [1], [2] while deficits in myocardial perfusion by the microcirculation can predict adverse cardiac outcome [3]. Although the implications of structural anomalies in the microvasculature are relatively well understood, the impact of changes in real-time perfusion is less well known. In part this is due to the low spatial and/ or temporal resolution of existing imaging modalities [4], [5] and the persistence of conventional contrast agents, which allow assessment of perfusion only through kinetic modelling [4]. A tool for the measurement of vascular structures with high spatiotemporal resolution and selective spatiotemporal activation would consequently be valuable for understanding dynamic processes in the microcirculation.

Super-resolution (SR) through optical switching and localization of individual fluorophores has revolutionized optical microscopy by enabling visualization of structures far below the wave diffraction limit [6], [7]. Similarly, in acoustics, ultrasound localization microscopy (ULM) has enabled imaging of the microvasculature below the diffraction limit to create functional SR images of microvascular structures [8], [9]. Microbubble-based SR ultrasound techniques have shown unprecedented levels of detail of the microcirculation in preclinical imaging of the kidney [10], [11], lymph node [12] and brain [13], while clinical applications include breast [14], lower limb [15] and transcranial brain imaging [16]. However, microbubble-based SR imaging requires seconds to minute-long acquisition times and cannot use a high bubble concentration without degrading the SR image quality as then individual bubbles cannot be localized. Some statistical approaches have been applied to permit higher concentrations and faster scan times to be used [17], [18], [19], [20], [21], but once a microbubble bolus has been injected, its concentration can

This work is licensed under a Creative Commons Attribution-NonCommercial-NoDerivatives 4.0 License.
For more information, see https://creativecommons.org/licenses/by-nc-nd/4.0/

only be regulated by deliberately destroying microbubbles with ultrasound or waiting for the bolus to become diluted by dispersion and partial clearance. Besides, it takes time for smaller vessels to be adequately perfused with microbubbles due to the low flow rates [22], [23] which further constraints controlling the dispersion of the contrast agent.

These fundamental limitations arise because microbubble contrast agents are not switchable in the same way as fluorophores in optical SR microscopy. Phase-change ultrasound contrast agents (*nanodroplets*), on the other hand, are acoustically switchable and enable on-demand sparse activation and deactivation. Nanodroplets are an order of magnitude smaller than microbubbles and can have a significantly longer half-life *in vivo* [25]. In their initial state nanodroplets are not detected by ultrasound; activation leads to their detection and deactivation leads to recondensation or disintegration [52], [53], [54]. This can be achieved at very high agent concentrations, both with and without flow, because not all nanodroplets are activated at the same time [24]. While higher-boiling-point droplets have been successfully activated with a laser pulse [27], low-boiling-point nanodroplets are activated and deactivated by the ultrasound pulse itself. The acoustic activation provides spatial selectivity of a region of interest in which nanodroplets are activated [49], [50]. Low-boiling-point nanodroplets can be fabricated by condensation of fluorocarbon microbubbles [26]. The lower the boiling point of a fluorocarbon, the lower is the energy required for nanodroplet activation and the higher is the probability of spontaneous vaporization. *In vivo*, octafluoropropane (OFP) droplets are metastable and require very low acoustic pressures for vaporization, if any [29]. Decafluorobutane (DFB) droplets are more stable but therefore require higher acoustic pressures for activation. Through tuning e.g., mixing gases or changing lipids, the metastable characteristics can be altered [30], [39], [40], [41], [51].Acoustic Wave Sparsely-Activated Localization Microscopy (AWSALM) [24] and fast-AWSALM [28] using such acoustically activatable nanodroplets have shown flow independent and sub-second SR imaging *in vitro* in a crossed tube phantom. An *in vivo* demonstration of these techniques has not yet been reported.

By refining AWSALM and fast-AWSALM imaging and combining these methods with three established fluorocarbon compositions and the ability to deliberately activate and silence nanodroplets, we demonstrate fast SR imaging with fast-AWSALM and for the first time selective SR imaging with AWSALM *in vivo*. In this study we quantify the pressure dependent droplet activation in a crossed tube phantom and illustrate droplet vaporization and silencing in the rabbit kidney. We show sub-second super-localization images of diastolic and systolic perfusion *in vivo* in the rabbit kidney with some microvascular detail and the selective imaging of specific vascular branches and detailed downstream microvasculature for acquisition times of up to 5.5 s. We compare fast-AWSALM with a microbubble acquisition demonstrating its potential for shorter acquisition times and discuss necessary future work.

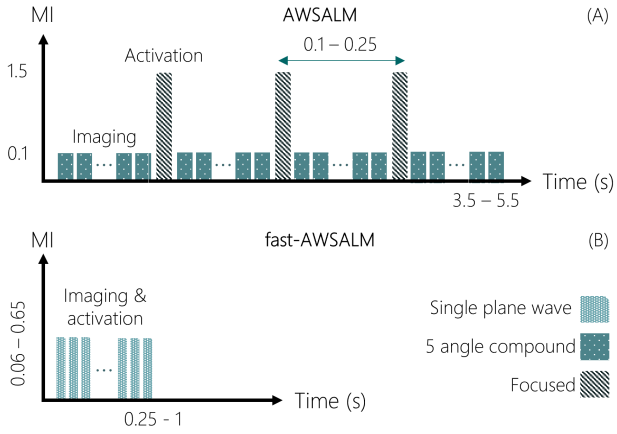

Fig. 1. (A) The AWSALM sequence alternates between focused activation and 5 angle plane wave imaging. In this work, the number of focal points (1 or 2) and f-number were varied. The acquisition time was between 3.5-5.5 s with a frame rate of 500 Hz. (B) fast-AWSALM combines imaging and activation through a single plane wave with a maximum acoustic pressure located at a depth of 15 mm. In this work, the acquisition time was between 0.25-1 s and the mechanical index (MI) was varied between 0.06-0.65, with frame rates up to 10,000 Hz.

II. Materials and Methods

A. AWSALM and Fast-AWSALM

AWSALM and fast-AWSALM both use acoustic transmissions to acoustically activate nanodroplets. Activation is caused by vaporization of the liquid core of a condensed nanodroplet and its subsequent expansion and formation of an oscillating microbubble. Deactivation, or *silencing*, is defined as the disappearance of the microbubble signal. The extent to which disintegration or recondensation occurs with AWSALM and fast-AWSALM is unknown. It is therefore possible that the phase change is predominantly one-time, and if the pressure is low it may be one-way. The two imaging techniques differ in their transmission sequence, acquisition duration and acoustic pressure. The latter is within recommended safety limits for diagnostic imaging. The AWSALM and fast-AWSALM pulse parameters used in this study are shown in Figure 1.

AWSALM separates the transmitted pulse sequence used for imaging from the pulses used for selective activation and deactivation of droplets. Nanodroplets are repeatedly activated and imaged. With every focused transmission at a high mechanical index (MI), a sub-population of the nanodroplets within a predefined region are activated. These are then imaged by low MI plane wave imaging sequences followed by localization and tracking in post-processing. With each activation sequence new microbubbles are formed and existing bubbles are silenced. This requires the use of long-lasting, medium-boiling point droplets [24].

In fast-AWSALM, the same plane-wave transmission simultaneously acoustically activates and images the contrast agent. With every transmission a sub-population of nanodroplets is vaporized. With every subsequent transmission a further sub-group of nanodroplets is vaporized and some of the previous bubbles are silenced. The survival time of a vaporized bubble depends on the acoustic pressure and the frame rate.

The use of metastable, low-boiling point droplets allows high concentrations to be used while still providing sparsity [28]. The pressure required is lower than that for the focused transmission in AWSALM.

B. Preparation of Nanodroplet Contrast Agent

For this study, three low-boiling-point fluorocarbon phase-change nanodroplets were made through condensation of phospholipid-coated microbubbles containing OFP (C_3F_8, b.p. $-36.7\,^\circ$ C), DFB (C_4F_{10}, b.p. $-1.9\,^\circ$ C) or a 1:1 volume mixture (C_3F_8:C_4F_{10}) (F2 Chemicals Ltd, UK). Microbubbles were fabricated as described by Lin et al. [31]. Nanodroplets were formed from them as follows: a phospholipid suspension was prepared by mixing 1,2-distearoyl-sn-glycero-3-phosphocholine (DSPC) and 1,2-distearoyl-sn-glycero-3-phosphoethanolamine-N-[methoxy (polyethylene glycol) - 2000] (DSPE-PEG-2000) (9:1, molar ratio) in phosphate-buffered saline, propylene glycol, and glycerol (16:3:1 by volume) for a total lipid concentration of 1 mg/ml. One ml of the solution was added to a 2 ml glass vial. The head space was then filled with C_3F_8, C_4F_{10} or a 1:1 volume ratio mixture. The mixture was prepared by filling 10 ml of a 20 ml syringe with C_3F_8 and the other half of the syringe with C_4F_{10} [41]. The fill pressure of each gas was regulated with a pressure gauge and set to 0.1 bar. Microbubbles were formed through 90 s of mechanical agitation (TP-103 amalgamator, Goldsmith & Reverse, Inc, USA). The vial containing microbubbles was subsequently submerged in a -10 $^\circ$ C water-salt solution where it was kept 10 minutes until needed. To fabricate droplets, the cooled microbubble solution was condensed inside a 1 ml syringe by manually pushing the plunger with the end sealed. The nanodroplet size ranges from 10 to 1000 nm. The mean diameter was previously measured at 119 nm [24]. The mean concentration of nanodroplets was $5.5 \cdot 10^9$ nanodroplets/ml compared to $6 \cdot 10^9$ microbubbles/ml [48]. Droplets from a single vial were used for up to 30 minutes.

C. Ultrasound Scanner

Experiments were conducted with a Verasonics Vantage 256 ultrasound research platform and a L11-4v linear array. The MI was calibrated in a water tank with a 0.2 mm needle hydrophone (Precision Acoustics, UK) and derated assuming a soft tissue attenuation coefficient $a_0 = 0.5$ dB/(MHz·cm).

D. Ultrafast Imaging Sequence

Two different transmission sequences were used (Figure 1). For AWSALM, the imaging part of the sequence consisted of 5 angle compounding single cycle plane waves at MI = 0.1 (pulse centre frequency = 4 MHz), giving a compounded frame rate of 500 Hz for imaging. A twenty cycle focused transmission at MI = 1.5 (centre frequency = 4 MHz) and frame rate of 50 Hz was used for vaporization. The number of focal depths was varied between 1 or 2, the focus depth was manually selected between 5-30 mm, the lateral focus position was selected between -15 to 15 mm. The number of activation/imaging cycles was 25 and the total number of frames acquired ranged between 1,530 to 2,280. The total duration of an AWSALM acquisition was between 3.5-5.5 s; of which approximately 80% was for imaging and 20% for activation.

The fast-AWSALM sequence consisted of single-angle, single-cycle plane wave imaging (centre frequency = 4 MHz) and frame rates between 2,000-10,000 Hz. The peak MI measured at 15 mm depth was varied between 0.06-0.65 for optimization. The total duration of each fast-AWSALM acquisition was between 0.25-1 s. During a single acquisition, the MI was not changed. A conservative minimum arbitrarily chosen interval of 20 s was maintained between fast-AWSALM acquisitions.

E. Super-Localization Pipeline

The radio frequency data were reconstructed with a delay-and-sum beamformer. A cross-correlation based rigid motion compensation and time gain compensation correction were applied prior to Singular Value Decomposition (SVD) clutter suppression. The AWSALM dataset was SVD filtered separately for each stack of images, whereas the fast-AWSALM dataset was filtered with all frames at once. For the comparison between fast-AWSALM and microbubbles a differential clutter filter with a lag of five frames was used instead of SVD. Note, in the caption of the figures the sum of the filtered data describes the clutter filtered data, whereas the sum of B-Mode describes the unfiltered data. Subsequently, the clutter-free data were filtered with an axial-temporal Wiener noise filter and a low-pass 3D convolutional filter. For the images of rabbit kidney acquired *in vivo*, a region of interest was drawn manually around the renal vasculature for each acquisition. All subsequent steps of the localization are based on previous work [8], [24]. First, 20 vaporized droplets were manually selected to configure the system's point spread function (PSF). Bubbles were localized in subsequent frames to create a velocity map based on cross-correlation with the PSF. Tracks were estimated and regularized using a combination of Kalman filter and graph-based assignment [32]. For AWSALM, the interruptions to the image sequence by the focus transmissions were accounted for.

F. In Vitro Crossed Tube

Vaporization of the three different fluorocarbon nanodroplets was first assessed in a microvascular flow mimicking phantom with the low MI fast-AWSALM sequence. The setup consisted of two crossing cellulose tubes (Hemophan Membrana, 3M, Minnesota, USA) with an inner diameter of 200 ± 15 μ m. The crossed tube phantom was submerged in $37 \pm 0.2\,^\circ$ C warm water inside a 20 L water tank. The volume flow was 30 μ l/min in each tube, resulting in a mean flow velocity of 16 mm/s. 0.5 ml of droplet solution was diluted in 15 ml of water. The centre of the crossed tubes was positioned at a depth of 15 mm with flow entering the field of view from the tube inlets furthest away from the transducer. The total acquisition time was 1 s with a frame rate of 5,000 Hz. Nanodroplet activation was quantified on unfiltered

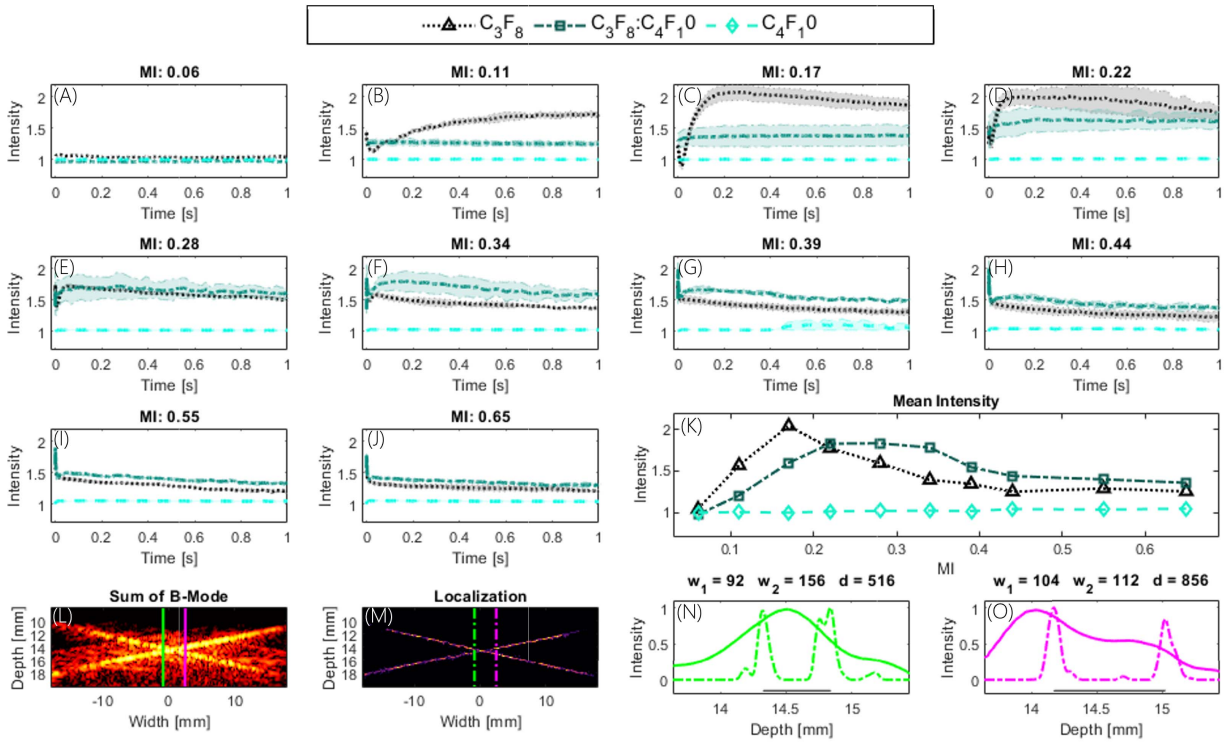

Fig. 2. (A-J) Mean intensity of the crossed tubes over time and (K) as a function of MI for different nanodroplets. (L,M) sum of B-Mode and super-localization. (N,O) normalized intensity profile across green and magenta lines in (L,M). The full width at half maximum is described as w_1 or w_2 and d is the distance between the two peaks of the crossed tubes marked by the green or pink line. Both the C_3F_8 and mixed-gas droplets, but not the C_4F_{10} droplets could be activated with plane waves at MI between 0.17 and 0.65 (K). Vaporized bubbles burst rapidly at MI>0.34.

gray scale images by measuring the mean intensity of the tubes with a manually defined region of interest as a surrogate for vaporization activity. The intensity was normalized with respect to the MI and by the C_4F_{10} acquisition at MI = 0.06. Measurements were repeated 3 times. Supplementary video 1 shows the droplet activation in the crossed tubes with AWSALM and fast-AWSALM. For visualization purposes the videos show very diluted concentrations. The concentration for the top video is 10^6 of C_4F_{10} nanodroplets. The concentration for the bottom video is 10^5 of C_3F_8:C_4F_{10} nanodroplets.

G. Renal Imaging in vivo

Imaging was performed on the left kidney of anaesthetized specific-pathogen-free male New Zealand White (NZW) rabbits. All experiments complied with the Animals (Scientific Procedures) Act 1986 and were approved by the Animal Welfare and Ethical Review Body of Imperial College London. Six rabbits (HSDIF strain, mean age 13 weeks; mean weight 2.4 kg; Envigo, UK) were sedated with acepromazine (0.5 mg/kg, i.m.) and anaesthetized with medetomidine (Domitor, 0.25 mL/kg, i.m.) plus ketamine (Narketan, 0.15 mL/kg, i.m.). The anaesthesia was maintained for up to 4 hours with administration of 1/3 of the initial medetomidine and ketamine dose every 30 minutes. Nanodroplet contrast agents were injected as a bolus of up to 0.3 ml/injection and a total of 1 ml/animal. Pentobarbital (0.8 ml/kg) was used for euthanasia. To access the renal vasculature, the rabbits were shaved and positioned supine. Mechanical ventilation was given at 40 breaths/minute; body temperature was maintained with a heated mat. Heart rate and oxygenation were continuously monitored.

III. Results

A. In vitro Crossed Tube Evaluation

The changes in mean image intensity over time due to the vaporization of fluorocarbon nanodroplets (C_3F_8, C_3F_8:C_4F_{10} and C_4F_{10}) in a crossed tube phantom with flow are shown in Figure 2 (A-J). For C_3F_8 the mean image intensity increased at MI = 0.11 and peaked at MI = 0.17 as shown in (K). For the mixture a first substantial increase in intensity is seen at MI = 0.17 and its peak is at MI = 0.28. At MI = 0.06 nanodroplets did not vaporize, and C_4F_{10} nanodroplets could not be vaporized with plane-waves at 37 ° C over the entire MI range tested. Repeated transmission at higher acoustic pressures caused a drop in intensity beyond MI = 0.34, suggesting more silencing of the vaporized droplets at higher MIs. Figure 2 (L-O) show the images and normalized intensity profiles across two different lines of the sum of the B-Mode and super-localized results respectively. The crossed tubes (N) can be resolved over a distance smaller than the axial direction of the measured PSF (574 μ m). The example (L-O) is taken from an acquisition with C_3F_8 nanodroplets at MI = 0.11.

B. Vaporization, Lifetime and Silencing

The difference between microbubble and nanodroplet spatio-temporal features and the influence of the imaging sequence in the rabbit kidney are shown in Figure 3.

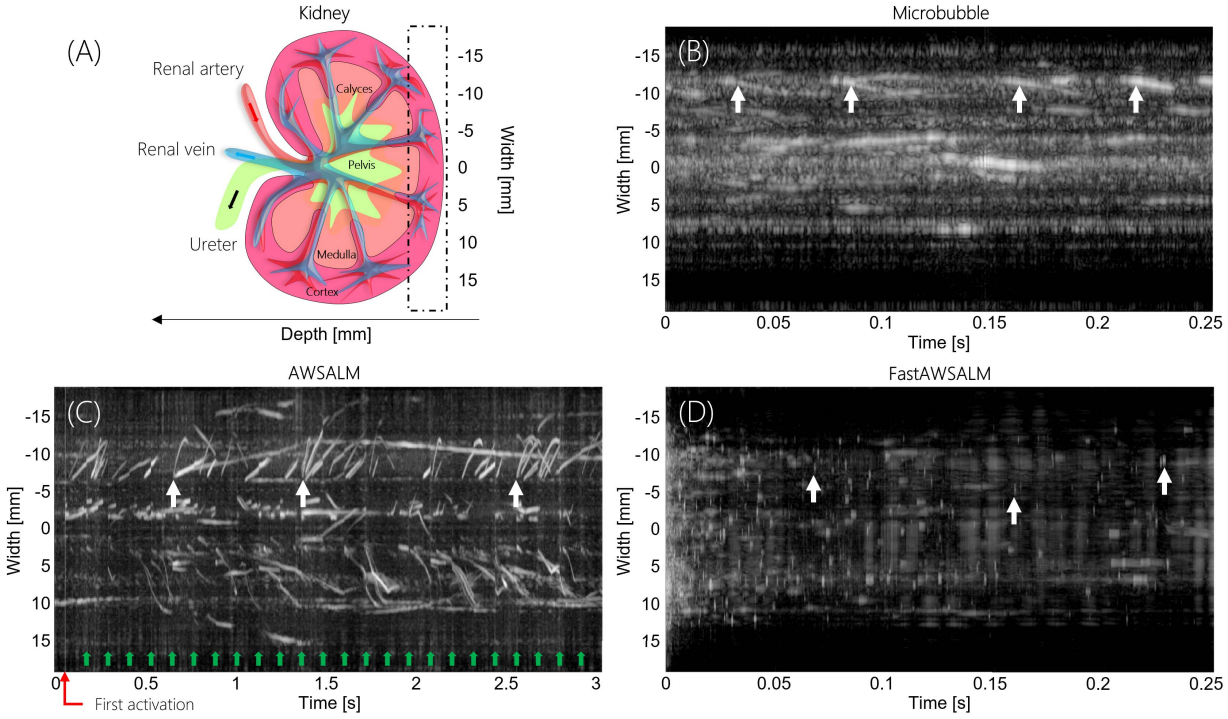

Fig. 3. Spatiotemporal imaging of nanodroplet dynamics *in vivo* in the rabbit kidney with conventional contrast, AWSALM and fast-AWSALM. The lateral-temporal signal of a maximum projection in the depth direction of the upper cortex of the rabbit kidney, as illustrated in (A, dashed box), obtained using (B) microbubbles, (C) AWSALM, (D) fast-AWSALM. Bubble tracks are visible in (B) and (C) as indicated by white arrows. Sparse activation and silencing of droplets can be observed in (D, white arrows). The lifetime from vaporization to silencing ranges from a few to dozens of transmissions. The first vaporization sequence of AWSALM is marked by the red arrow below (C). A total of 25 activation sequences were transmitted each marked by a green arrow. Note that (B/D) is from a single angle plane-wave acquisition of 0.25 s duration and 5 kHz frame rate, whereas (C) is from a five-angle compounding acquisition of 3 s duration and 0.5 kHz frame rate. In (C) C_4F_{10} and in (D) C_3F_8:C_4F_{10} nanodroplets were used.

Figure 3 (B-D) shows the lateral-temporal signal from a maximum projection taken in the depth direction of the upper cortex of the rabbit kidney (A, dashed box). Each acquisition was acquired after a bolus injection of 0.1 ml of contrast agent. (B,D) were acquired with a frame rate of 5 kHz and (C) with 0.5 kHz. The concentration of microbubbles in the maximum projection image is very high and only a few isolated bubble traces can be seen in parts of Figure 3 (B). Figure 3 (C) shows repeated activation of droplets with the AWSALM sequence. Droplets are sparse and the individual tracks are easily identifiable (examples shown by the white arrows). The red arrow below Figure 3 (C) marks the first activation event, the green arrows mark all consecutive events. The recurring activation of droplets led to a sparse, continuous stream of new bubbles. Figure 3 (D) presents the sparse activation and silencing of nanodroplets with fast-AWSALM, with exemplar events illustrated by white arrows. The lifetime of bubbles formed from nanodroplets ranged from a few transmissions/ milliseconds to dozens of transmissions/ milliseconds. If the imaging MI was low, many vaporized droplets persisted over multiple transmissions and some can persist until they exit the imaging plane. The number of vaporization events was highest at the beginning of the acquisition and reduced over time.

C. Contrast on-Demand

The frame before and 15 frames after the first activation of C_4F_{10} nanodroplets with AWSALM is shown in the

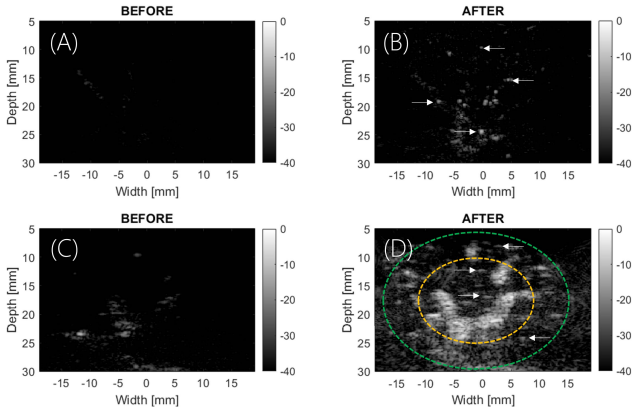

Fig. 4. *In vivo* imaging of rabbit kidney with nanodroplets. Filtered images before (A) and after (B) the first activation sequence of AWSALM (C_4F_{10}, single focus point at depth of 25 mm). The activation is focused on a single depth and bubbles are sparse. Filtered images before (C) and after (D) the first activation of fast-AWSALM (C_3F_8:C_4F_{10}). Activation occurs over the whole depth-range imaged. The white arrows in (B) and (D) show examples of isolated microbubbles. The yellow circle indicates the approximate location of the medulla and the green circle indicates the approximate location of the cortex.

clutter-filtered images in Figure 4 (A,B). It shows the local activation of C_4F_{10} with a single focus point at 25 mm depth and subsequent occurrence of sparse bubbles in the medulla of a rabbit kidney. The white arrows indicate the location of exemplar microbubbles. The bubble density can be varied through the number of focus points and selection of the

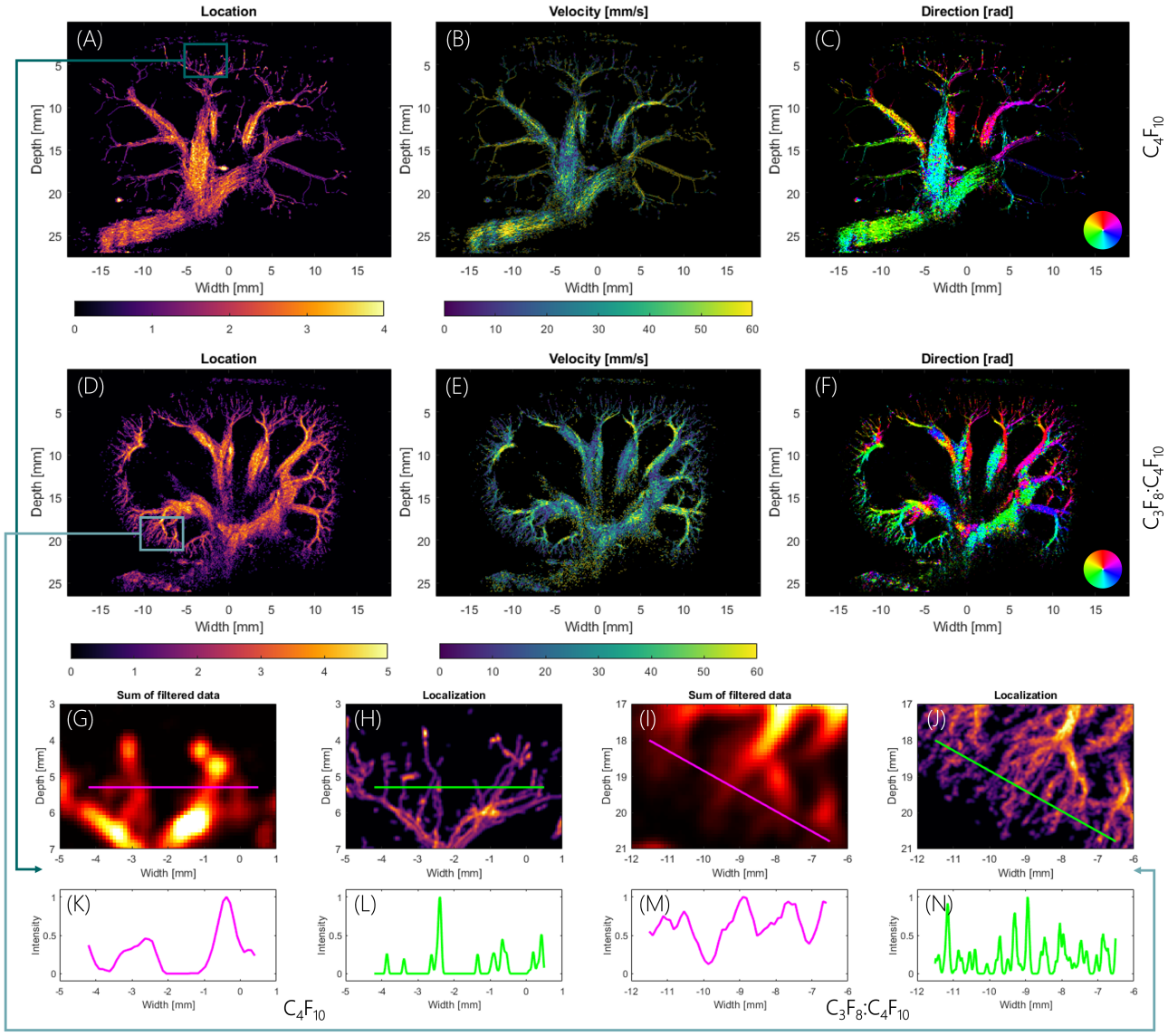

Fig. 5. AWSALM super-resolution square rooted density map of localization (A,D), absolute flow velocity (B,E) and direction of droplet movement (C,F) in two rabbit kidneys. (A-C) presents a 3.5 s acquisition with C_4F_{10} nanodroplets (3 s, imaging; 0.5 s activation). The focal region was at a depth of 25 mm and lateral positions from −4.8 mm to 2.4 mm and activation was repeated 25 times. (D-F) show the maps of density, velocity and direction from an acquisition of C_3F_8:C_4F_{10} droplets. Total duration of 5.5 s, of which 4.5 s and 1 s was used for imaging and activation respectively. Two focal zones at depths of 16 mm and 23 mm were used over a lateral range of −7.2 mm and 6.3 mm and activation was repeated 25 times. (G-N) show a zoomed in view with corresponding normalized intensity profile.

gas mixture. Figure 4 (C,D) demonstrates the activation of C_3F_8:C_4F_{10} nanodroplets with the fast-AWSALM transmission sequence over a larger field of view than achieved with AWSALM. The distribution of microbubbles is denser in the medulla (large vessel) than in the cortex (small vessel) of the rabbit kidney. In the larger vessels, speckle patterns develop as indicated by the red arrow. In Figure 4 (C) a small number of bubbles can be observed prior to the activation pulse, likely due to spontaneous vaporization.

D. In vivo SR With AWSALM

The AWSALM SR sequence was applied to two rabbit kidneys; the results (Figure 5) demonstrate the versatility of the method. The top row maps the square rooted density of localized C_4F_{10} droplets (A), their absolute velocity (B) and their direction (C). Data were acquired in 3.5 s, of which 3 s was imaging and 0.5 s was activation, respectively. Nanodroplets were activated at a focal depth of 25 mm, with 25 focused transmissions between −4.8 mm and 2.4. The bottom row shows a C_3F_8:C_4F_{10} acquisition with 1 s of activation and 4.5 s of imaging. Activation occurred at two focal depths, the first at 16 mm and the second at 23 mm, with 25 focused transmissions between lateral positions of −7.2 mm and 6.3 mm. The peak velocities were 60 mm/s and both arterial blood flow and venous return could be quantified (see supplementary Video 2 and 3).

In Figure 5 (L,N) mean vessel width at full width half maximum (FWHM) is 121 ± 40 μ m for 9 vessels with an average of 5.73 peak number of localizations per vessel. Vessels reconstructed from at least 4 localizations were

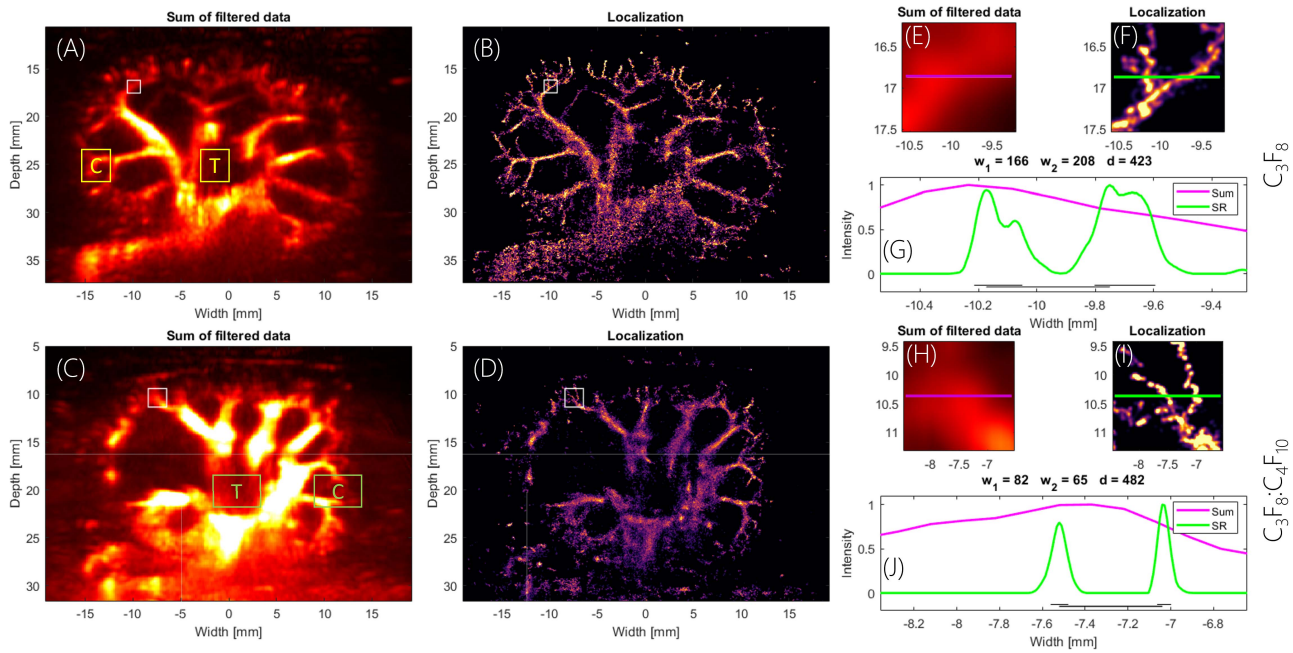

Fig. 6. (A,C) Fast-AWSALM sum of filtered data, (B,D) SR density maps and (G,J) normalized intensity profile in region of interest shown by white boxes in (A-D). (E,F,H,I) zoomed in view of the region of interest. Images on the top (A,B,E-G) represent an acquisition with C_3F_8 nanodroplets (0.25 s, simultaneous imaging/activation). (C,D,H-J) show the results of imaging with the gas-mixture (C_3F_8:C_4F_{10}) droplets, obtained with 1 s of simultaneous imaging/activation. Data were acquired with a frame rate of 5,000 Hz and at MI = 0.22. In (G, J), the full width at half maximum is described by w_1 or w_2 and d is the distance between the peaks marked by the green line. Boxes C and T mark region for the contrast to tissue ratio measurement.

considered. Resolution was therefore increased by a 4-fold in the lateral and axial directions compared to the PSF at 4 MHz (543/ 530 μ m). The smallest distance between two fully resolved adjacent vessels was 115 μm, which is smaller than half the wavelength (192.5 μm) at 4 MHz. Three times the number of vessels could be detected compared to conventional US.

E. In vivo SR With Fast-AWSALM

Sub-second super-resolution imaging was achieved with the fast-AWSALM sequence and C_3F_8 droplets (Figure 6 A,B,E-G) and with C_3F_8:C_4F_{10} droplets (Figure 6 C,D,H-J). Figure 6 (A,C,E,H) show the linear sum of the signal after filtering. Figure 6 (B,D,F,I) show the super-localized maps and Figure 6 (G,J) each show the respective normalized intensity profiles. The C_3F_8 droplet acquisition was acquired in 0.25 s and the C_3F_8:C_4F_{10} acquisition was acquired in 1 s. For the C_3F_8:C_4F_{10} mixture acquisition the majority of the signal was detected in larger vessels and vaporization events were mostly sparse and not connected in the cortex despite the longer duration. The signal from C_3F_8 droplets, on the other hand, was evenly distributed in the core and cortex region of the kidney. Both acquisitions reveal microvascular detail that is not visible without super-localized imaging (Figure 6 G,J). The accumulation of localization is shown in supplementary Video 2. The contrast to tissue ratio was 9 dB and 6.9 dB for Figure 6 A and C, respectively.

The smallest measured distance between two adjacent vessels was 423 μm (Figure 6). The mean width was 130 $\pm$68 μ m for 4 vessels and 2.8 number of localizations per vessel. This again yields a similar 4-fold improvement in the lateral and axial directions compared to the PSF at 4 MHz (487/ 574 μ m). Note, the cut-off threshold for the minimum number of localizations per vessel (2) was half of the value used for AWSALM (4). This decision was made due to a much smaller total number of localizations.

F. Selective Super-Localization

The deliberate activation and deactivation of C_3F_8:C_4F_{10} mixture nanodroplets can be demonstrated through the selective activation of different regions of the microvasculature in the same imaging plane, as shown in Figure 7 (A-C). In Figure 7 (A, D) shows perfusion of the left branches, Figure 7 (B, E, F) perfusion of the entire renal vasculature and Figure 7 (C. G) structures on only the right side of the kidney. In Figure 7 (D-G), the direction of flow in a region of interest is shown. The dotted white lines in Figure 7 (A-C) show the focal points.

G. Sub-Second Super-Localization

The broad activation of nanodroplets with fast-AWSALM can be seen in Figure 8 (D-F), which show two sub-second visualizations of the rabbit kidney and microvascular structures during systolic (E) and diastolic (F) perfusion. Data were acquired at 5 kHz with C_3F_8 droplets over a 1 second period. Images were generated from a subset of the same 1 s. (A-C) show a reference acquisition with microbubbles. Each SR image (E, F) was produced over a duration of 0.25 s in the same cardiac cycle. In Figure 8 (G-L), corresponding intensity profiles of the localization maps of two regions of

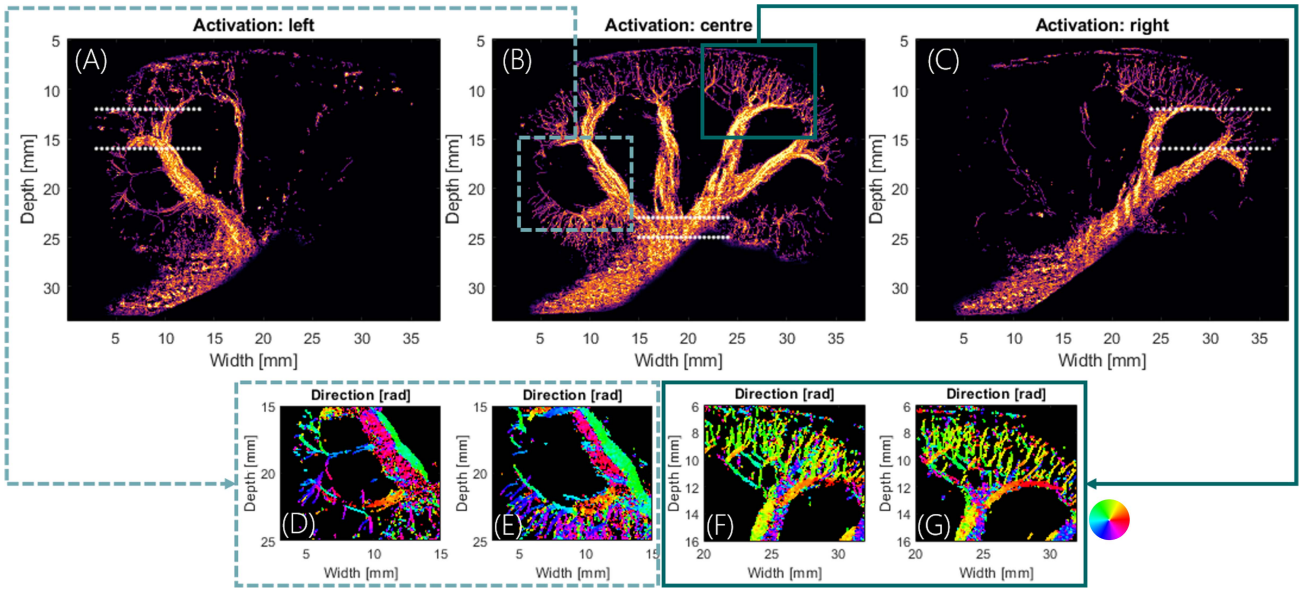

Fig. 7. The deliberate activation and deactivation of C_3F_8:C_4F_{10} mixture nanodroplets with AWSALM can highlight different regions of the renal vasculature. (A-C) demonstrate the selective activation of different regions of the microvasculature in the same plane. (D,E) and (F,G) show flow direction in a region of interest for activation regions on the left (D), in the middle (E,F) and on the right (G), respectively. The three regions of the vasculature were each imaged for 4.5 s with 25 intermittent activations for a total acquisition duration of 5.5 s. Note, the activation is diffraction limited which allows targeting only larger vessels. The dotted white lines (A-C) show the focal points of the activation sequence.

interest are shown. Some smaller vessels that are perfused during systole appear not to be perfused during diastole. The number of resolved adjacent vessels in the intensity profiles in (J,K,L, purple) is 20, 13 and 10 respectively. The nanodroplet acquisition yields more vascular detail compared to the microbubble acquisition in the majority of the image. In lateral regions marked by the yellow arrow, the microbubble acquisition is superior. The localization map over time using nanodroplets can be seen in supplementary Video 3.

IV. Discussion

The generation of ultrasound SR images poses two key challenges: how to obtain a sufficient contrast agent concentration to keep acquisition times low without compromising the ability to isolate individual microbubble signals; and how to actively manipulate contrast agent concentration in the blood stream in real time. In this study we demonstrated, for the first time, fast and selective super-localization imaging of microvascular flow *in vivo* with AWSALM and fast-AWSALM using acoustically activatable nanodroplets. This was achieved by refining the previously published AWSALM and fast-AWSALM imaging sequences and their combination with three established fluorocarbon compositions and the prior knowledge that nanodroplets can be activated deliberately. We demonstrated the capability of AWSALM to selectively visualize the downstream microcirculation of a specific vessel branch, and the feasibility of fast-AWSALM to capture the systolic and diastolic events in the kidney from a sub-second acquisition; with more vascular detail compared to microbubbles. We achieved this using acoustic pressures within recommended safety limits. The mixing of gases provided a level of control that was necessary for the first *in vivo* translation of AWSALM and fast-AWSALM and to solve the two key challenges of SR imaging.

Acoustically activatable nanodroplets enable generation of ultrasound contrast signals on demand, with control in both space and time as shown in Figure 5 and Figure 6. By fast activation/ destruction and imaging of these nanodroplets, AWSALM and fast-AWSALM offer the unique capability of generating both selective (Figure 7) and fast (Figure 8) super-localization microscopic images of the microcirculatory region of interest. Conventional microbubble-based ULM is not selective and is slower. At the same time, the techniques retain some key advantages of medical ultrasound, including deep tissue penetration compared to optical techniques where penetration depth is an issue. The penetration depth of AWSALM and fast-AWSALM imaging is mainly limited by the acoustic pressure required for vaporization. Compared to x-ray or computed tomography (CT) angiography, AWSALM and fast-AWSALM use non-ionizing radiation and the contrast injection is less invasive. The microvascular contrast and achievable resolution also make the proposed techniques stand out among other clinical imaging modalities including CT, magnetic resonance imaging (MRI) and positron emission tomography (PET) [4].

The acoustic activation and deactivation of nanodroplets (Figure 4, supplementary Video 1) is a unique feature that other non-invasive imaging modalities do not offer. It avoids the issues in perfusion imaging, that contrast agent kinetic modelling can suffer from effects of variable transit delays or fitting errors [33]. Recent work has demonstrated the use of blinking acoustic nanodroplets (BAND) which can be repeatedly activated with higher pressures and this approach is capable of being fast and selective [42]. However, compared to BAND, AWSALM and fast-AWSALM can be achieved at higher frame rates, with fewer activation transmissions (AWSALM) and lower acoustic pressures. However, even with low-boiling point nanodroplets, not all droplets are vaporised, and not all bubbles from vaporised droplets are silenced.

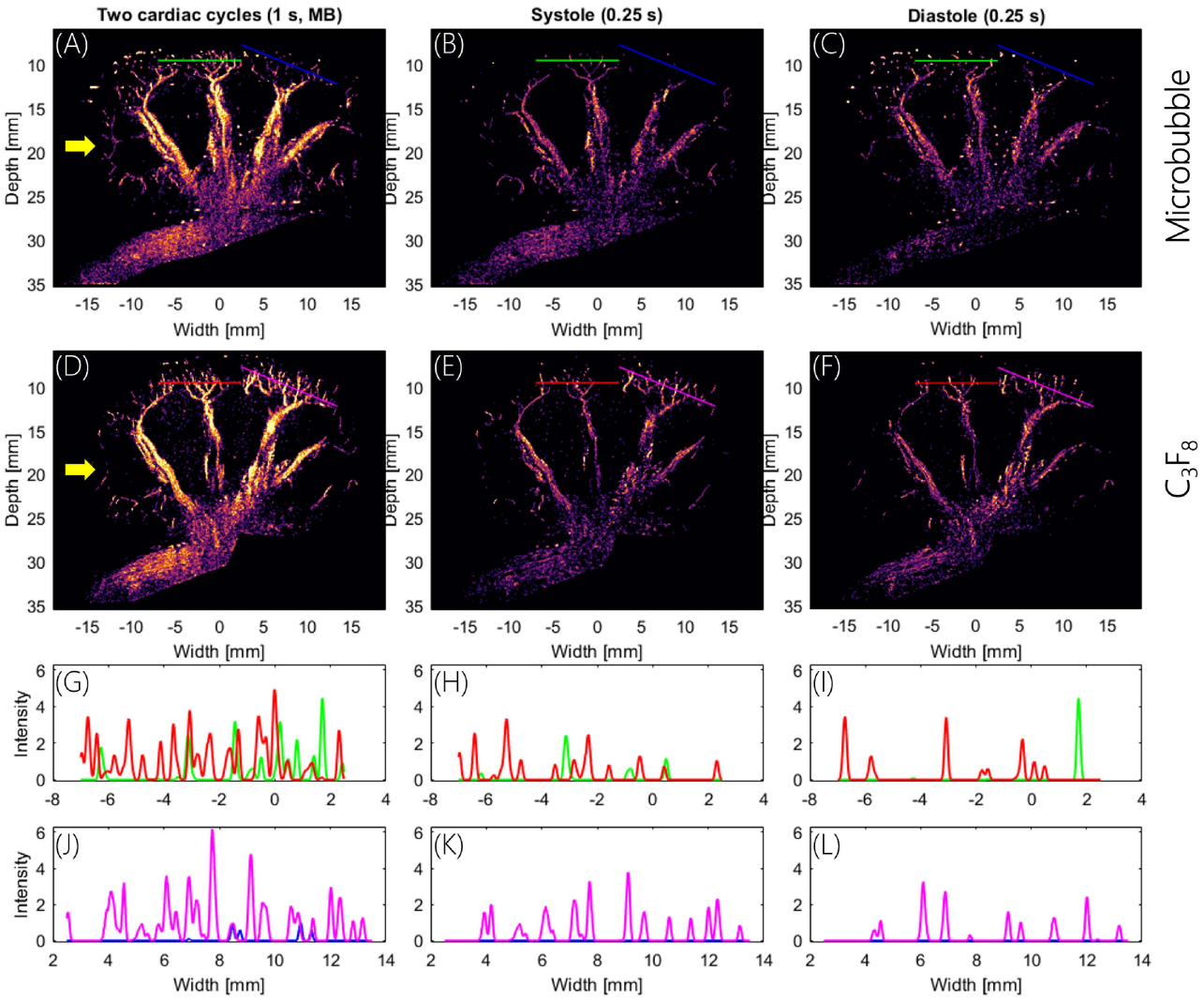

Fig. 8. The activation of C_3F_8 nanodroplets over the full field of view with fast-AWSALM can create sub-second visualizations of the renal vasculature, allowing separation of 0.25 second segments of systole (E) and diastole (F) from a single 1 s long acquisition (D). (A-C) show the kidney from a reference measurement with microbubbles. The reference microbubble acquisition was acquired after the nanodroplet acquisition. The parts of cardiac cycle were selected manually based on renal blood flow measurement. Different regions of the microvasculature are perfused with bubbles during the cardiac cycle. (G-L) show regions of interest (line) with corresponding intensity profiles. Vessel number and location change between systolic, diastolic and two cardiac cycle perfusion. In most regions the nanodroplet acquisition contains more detail than the microbubble acquisition. On the side marked by the yellow arrows the microbubble acquisition shows more detail.

The fact that vaporized droplets are indeed silenced due to subsequent ultrasound transmission is evident in Figure 3. At a frame rate of 5 kHz and with a maximum velocity of 60 mm/s in the medulla (max. velocity in Figure 5), the maximum displacement per frame is 1.2e-05 m or 12 μm. This is well within the elevational thickness of the ultrasound beam even after multiple transmissions and the bubble disappearance cannot be explained by out of plain motion. The control over the activation and deactivation is limited by the acoustic pressure, the possibility that the deactivation transmission vaporizes new droplets, and that the ultrasound energy is only applied in one small and thin 2D slice at a time.

Establishing the correct gas mix was consequently needed to achieve the presented results as it provides an additional mechanism of control. The C_4F_{10} nanodroplet is the most stable and can only be used with high acoustic amplitude activation. This offers the best control of activation but takes longer for data acquisition. The relatively high activation and silencing pressure and potential bioeffects still need to be explored. The C_4F_{10} nanodroplet can only be used with AWSALM. The C_3F_8 nanodroplet is the opposite and offers easy activation with very low MI required. The C_3F_8 nanodroplet enables simultaneous plane wave activation and imaging and thus SR imaging can be very fast. At low MI the low activation threshold of the C_3F_8 nanodroplet enables one-way phase change with exclusive activation of new nanodroplets but little silencing. However, the low activation threshold and the spontaneous activation through thermal pressure also reduce the level of control over the activation. The C_3F_8 nanodroplet can be used with AWSALM and fast-AWSALM but is better suited for fast-AWSALM. The C_3F_8:C_4F_{10} mixture nanodroplet presents a compromise between control and activation threshold. As such the droplet can be vaporised with a much lower MI than C_4F_{10} alone and offers better control

over the activation than C_3F_8 alone. The pressure required for activation is high enough for nanodroplet silencing. The activation of the C_3F_8:C_4F_{10} is achievable by either focused or plane wave imaging and can be used with AWSALM and fast-AWSALM without constraints.

The selective activation of single branches allows direct measurement of blood velocity and vessel density or other key vascular performance indicators in the dependent vasculature but is only possible with AWSALM. AWSALM SR could be used in the clinic for acute renal failure or transplant function, where contrast-enhanced ultrasound is already a widely applied method [33], [34]. Note, that the selectivity of the region that is being activated is limited by the diffraction limit. The acoustic pressure may exceed the vaporization threshold both in the region of interest and in non-focal regions nearby. The vessel structures that can be isolated are typically larger branches as shown in Figure 7. Specific activation of vessel regions may be more challenging in other organs and nearby vessels may be weakly associated with each other which warrants further investigation.

Besides imaging the kidney as shown in this work, the deliberate activation of contrast agents could be applied to ultrasound angiography through minimal-invasive injection/activation to detect arterial stenosis in real-time [45]. The main limitation here will be heterogeneity in tissue attenuation and an inhomogeneous pressure field. With a focused transmission the region of highest pressure tapers towards the focal point. With unfocused e.g., plane wave transmission pressure is highest in the centre and at the elevational focus. It diminishes with depth, in the near field and can be asymmetrical. For example, with a plane wave transmission and a soft tissue attenuation coefficient of $a_0 = 0.5$ dB/(MHz·cm) the measured peak pressure of the L11-4v is at 15 mm. At 5 mm the acoustic pressure is about 20% lower and at 25 mm the pressure is about 30% lower. The highest region of pressure is not at the centre but at the probe edge where side lobes are generated and about 20% higher than at the elevational focus in the centre [57]. This is true at zero degree transmission but changes when transmitting with a tilted angle. In addition, tissue attenuation my vary between $a_0 = 0.03$ - 4 dB/(MHz·cm) within the plane of view [56]. This inhomogeneity can interfere with nanodroplet activation and impede the maintenance of the appropriate or desired local concentration. The decrease in pressure with depth could be compensated for by increasing the transmission voltage. Figure 1 shows that a minimum MI of 0.11 is required to activate C_3F_8 nanodroplets. These nanodroplets can be used for both the fast-AWSALM and AWSALM application. The MI of the imaging setup at 50 mm depth with 40 V transmission and plane wave imaging is 0.1. For a focused or weakly focused wave the MI can be much higher. AWSALM and fast-AWSALM imaging deeper than 25mm as presented here is possible. Further investigation is required to establish the maximum penetration depth of both methods. Another limitation of nanodroplets is the potential for harmful bioeffects. Nanodroplets can extravasate and have been used as inertial cavitation nuclei in therapeutic applications, which for example can lead to microvascular leakage and cell injury [43], [44]. The effects of sparse but repeated acoustic nanodroplet vaporization need to be carefully investigated to make FDA approval possible, which is a requirement for the translation to human use.

AWSALM and fast-AWSALM can acquire images faster than microbubble-based ULM due to the higher concentration of contrast agents that can be injected at once (Figure 8). Note, that the difference in the level of detail in the region of interest between the microbubble and nanodroplet acquisition could have been caused by motion of the animal between the measurements (probe was fixed) or by the spatiotemporal features of nanodroplets (Figure 3) that facilitate their detection. In the spatiotemporal domain, activated droplets become lines with AWSALM and highly distinguishable short-lived dots with fast-AWSALM. These features could significantly speed up the detection algorithm. For example the slope of a bubble track in the spatiotemporal domain also corresponds to the axial or lateral velocity of the bubble. At the same time nanodroplets may extravasate into extravascular space which can lead to unwanted localizations outside the vasculature. Persistence and vessel continuity need to be monitored to indicate whether droplets have extravasated or not. This is a disadvantage compared to conventional contrast agents where enhanced permeability and effects of poor retention are minimal.

A major limitation of SR ULM is tissue motion. Tissue motion will impact fast-AWSALM and AWSALM too, but each differently. While fast-AWSALM uses very short acquisition times and very high frame rates, AWSALM is non continuous. The breaks between imaging sequences may affect correction of large motion e.g., for cardiac SR imaging. Some changes to the imaging sequence might be required to minimize motion artefacts such as higher frame rates, wider transmit beams, fewer focused transmissions, or a longer period of continuous flow imaging [55]. Droplet vaporization and imaging may be asynchronous. Due to the slow flow in the microvasculature two adjacent vaporized droplets might be resolved as a single bubble. Increasing the frame rate not only reduces motion artefacts but also reduces the ambiguity during detection of close by droplets [27]. However, the improvement in recognizable detail in the SR image is limited by the localization accuracy with such high frame rates. Although tissue motion is detrimental to clutter suppression if using Singular Value Decomposition the unique characteristics of nanodroplets and their low spatiotemporal correlation with other scatterers may allow separation of very slow or stationary nanodroplet signal from tissue and from flow. This could facilitate monitoring of extravascular tissue [50].

We have shown in this study that the three different fluorocarbon nanodroplets can be vaporized in a microvascular flow mimicking phantom (Figure 3 and supplementary Video 1) and that the choice of droplet has a substantial impact on the SR imaging results (Figure 5) affecting the number of vaporization events (which can also be controlled by adjusting the MI and frame rate). Through the use of the C_3F_8:C_4F_{10} mixture the AWSALM sequence could be used at a significantly lower MI, while providing much greater stability and control for the fast-AWSALM sequence compared to C_3F_8 droplets. However, the main limitation of fast-AWSALM in the *in vivo* experiments was variability in the amount of vaporization generated by the

same ultrasound transmission. This might be due to the rate of depletion of the C_3F_8 species in C_3F_8:C_4F_{10} droplets [29]. The ability to activate changes over time (seconds) and the rate of change was different with each experiment. This was likely caused due to variations in gas composition. Tissue motion, uneven and spatially varying attenuation and the image application e.g., difference between the desired frame rate for kidney or cardiac imaging further diminish the control over nanodroplet vaporization with fast-AWSALM, and to a lesser extent with ASWALM. Changing the lipid shell [36], [39], [40], using mono-sized nanodroplets [37] and implementing real-time feedback to automatically adjust ultrasound parameters based on the received signals should be able to further improve the reproducibility of fast-AWSALM. Heterogeneity in attenuation and local pressure might explain the uneven distribution of localization as seen in Figure 8. Specifically, lateral regions show less vascular detail compared to the proximal cortex region at the top of the image. Additionally, imaging MIs too high or too low do not generate satisfactory results. The former does not vaporize enough droplets, the latter silences bubbles too fast. The very short acquisition time of fast-AWSALM causes the number of localizations per vessel to be low, and this increases the uncertainty when determining the size of a vessel. Over the course of the experiments, we could observe a decrease in heart rate of approximately 30%. Blood oxygenation, temperature and ventilation/perfusion stayed consistent.

When comparing AWSALM and fast-AWSALM, the latter is a closer counterpart of the PALM system for optical SR. AWSALM uses separate pulses for acoustic activation and imaging. With this configuration it is possible to track the vaporized bubbles and generate flow velocity measurements. Fast-AWSALM uses the same plane wave pulses of medium MI for both acoustic activation and imaging. With this configuration some vaporized bubbles are quickly silenced, as seen in Figure 3, making flow tracking more difficult (some bubbles are not silenced). In this study we have not generated a map of velocities with fast-AWSALM. Further investigation is needed to explore the tracking of activated droplets that are not immediately silenced by the subsequent pulse. The contrast to tissue ratio and resolution with the current single-angle plane wave fast-AWSALM sequence (Figure 6) might be improved with angle compounding (activated nanodroplets can sustain multiple transmissions as shown in Figure 3). Compared to microbubble-based approaches, nanodroplet-based approaches offer better control of where and how much bubble signal is generated, achieving flexible and faster SR imaging in even low-flow environments, as evidenced in Figure 7 and 8. The clinical benefit of nanodroplet-based methods compared to microbubble-based methods remains to be explored. We believe that nanodroplets are likely to be particularly important in cases where vascular network connectivity up or down stream of the region of interest is of importance, where rapid imaging is required, e.g., due to significant motion, or in areas of slow flow, e.g., in tortuous tumours or where quantifying perfusion is important. In contrast, the microbubble-based approach is a simpler approach with already FDA-approved agents and is more suited for tissue with small motion such as the brain.

In conclusion, this work shows the feasibility of on-demand and sub-second SR imaging with acoustically activatable fluorocarbon nanodroplets for the selective real-time visualization of structural microvascular dynamics with AWSALM and fast-AWSALM. We demonstrated the feasibility of activating and silencing the nanodroplets at a relatively low MI, control of where (local or global) and when the activation of droplets takes place, flexibility over interleaving the activation and silencing pulses with imaging pulses, and the ability to change the vaporization threshold of the contrast agents. It is thus envisaged that the technique could be customized for a wide range of clinical or research needs.

REFERENCES

[1] R. Lugano, M. Ramachandran, and A. Dimberg, "Tumor angiogenesis: Causes, consequences, challenges and opportunities," *Cellular Mol. Life Sci.*, vol. 77, no. 9, pp. 1745–1770, May 2020.

[2] P. Carmeliet and R. K. Jain, "Angiogenesis in cancer and other diseases," *Nature*, vol. 407, no. 6801, pp. 249–257, 2000.

[3] J. Betancur et al., "Prognostic value of combined clinical and myocardial perfusion imaging data using machine learning," *Cardiovascular Imag.*, vol. 11, no. 7, pp. 1000–1009, 2018.

[4] M. Dewey et al., "Clinical quantitative cardiac imaging for the assessment of myocardial ischaemia," *Nature Rev. Cardiol.*, vol. 17, no. 7, pp. 427–450, 2020.

[5] T. M. Kierski and P. A. Dayton, "Perspectives on high resolution microvascular imaging with contrast ultrasound," *Appl. Phys. Lett.*, vol. 116, no. 21, 2020, Art. no. 210501.

[6] E. Betzig et al., "Imaging intracellular fluorescent proteins at nanometer resolution," *Science*, vol. 313, no. 5793, pp. 1642–1645, 2006.

[7] M. J. Rust, M. Bates, and X. Zhuang, "Sub-diffraction-limit imaging by stochastic optical reconstruction microscopy (STORM)," *Nature Methods*, vol. 3, no. 10, pp. 793–795, 2006.

[8] K. Christensen-Jeffries, R. J. Browning, M. X. Tang, C. Dunsby, and R. J. Eckersley, "In vivo acoustic super-resolution and super-resolved velocity mapping using microbubbles," *IEEE Trans. Med. Imag.*, vol. 34, no. 2, pp. 433–440, Feb. 2015.

[9] C. Errico et al., "Ultrafast ultrasound localization microscopy for deep super-resolution vascular imaging," *Nature*, vol. 527, no. 7579, pp. 499–502, Nov. 2015.

[10] S. B. Andersen et al., "Super-resolution imaging with ultrasound for visualization of the renal microvasculature in rats before and after renal ischemia: A pilot study," *Diagnostics*, vol. 10, no. 11, pp. 1–15, 2020.

[11] Q. Chen, J. Yu, B. M. Rush, S. D. Stocker, R. J. Tan, and K. Kim, "Ultrasound super-resolution imaging provides a noninvasive assessment of renal microvasculature changes during mouse acute kidney injury," *Kidney Int.*, vol. 98, no. 2, pp. 355–365, Aug. 2020.

[12] J. Zhu et al., "3D super-resolution U.S. Imaging of rabbit lymph node vasculature in vivo by using microbubbles," *Radiology*, vol. 291, no. 3, pp. 642–650, Jun. 2019.

[13] V. Hingot, C. Errico, M. Tanter, and O. Couture, "Subwavelength motion-correction for ultrafast ultrasound localization microscopy," *Ultrasonics*, vol. 77, pp. 17–21, May 2017.

[14] S. Dencks et al., "Clinical pilot application of super-resolution U.S. Imaging in breast cancer," *IEEE Trans. Ultrason., Ferroelectr., Freq. Control*, vol. 66, no. 3, pp. 517–526, Mar. 2019.

[15] S. Harput et al., "Two-stage motion correction for super-resolution ultrasound imaging in human lower limb," *IEEE Trans. Ultrason., Ferroelectr., Freq. Control*, vol. 65, no. 5, pp. 803–814, May 2018.

[16] C. Demené et al., "Transcranial ultrafast ultrasound localization microscopy of brain vasculature in patients," *Nature Biomed. Eng.*, vol. 5, no. 3, pp. 219–228, 2021.

[17] A. Bar-Zion, C. Tremblay-Darveau, O. Solomon, D. Adam, and Y. C. Eldar, "Fast vascular ultrasound imaging with enhanced spatial resolution and background rejection," *IEEE Trans. Med. Imag.*, vol. 36, no. 1, pp. 169–180, Jan. 2017.

[18] R. J. G. van Sloun et al., "Super-resolution ultrasound localization microscopy through deep learning," 2018, *arXiv:1804.07661*.

[19] J. Yu, L. Lavery, and K. Kim, "Super-resolution ultrasound imaging method for microvasculature in vivo with a high temporal accuracy," *Sci. Rep.*, vol. 8, no. 1, pp. 1–11, Dec. 2018.

[20] C. Huang et al., "Short acquisition time super-resolution ultrasound microvessel imaging via microbubble separation," *Sci. Rep.*, vol. 10, no. 1, pp. 1–13, Dec. 2020.

[21] L. Milecki et al., "A deep learning framework for spatiotemporal ultrasound localization microscopy," *IEEE Trans. Med. Imag.*, vol. 40, no. 5, pp. 1428–1437, Feb. 2020. [Online]. Available: https://pubmed.ncbi.nlm.nih.gov/33534705/

[22] K. Christensen-Jeffries et al., "Poisson statistical model of ultrasound super-resolution imaging acquisition time," *IEEE Trans. Ultrason., Ferroelectr., Freq. Control*, vol. 66, no. 7, pp. 1246–1254, Jul. 2019.

[23] V. Hingot, C. Errico, B. Heiles, L. Rahal, M. Tanter, and O. Couture, "Microvascular flow dictates the compromise between spatial resolution and acquisition time in ultrasound localization microscopy," *Sci. Rep.*, vol. 9, no. 1, p. 2456, 2019.

[24] G. Zhang et al., "Acoustic wave sparsely activated localization microscopy (AWSALM): Super-resolution ultrasound imaging using acoustic activation and deactivation of nanodroplets," *Appl. Phys. Lett.*, vol. 113, no. 1, Jul. 2018, Art. no. 014101.

[25] A. L. Y. Kee and B. M. Teo, "Biomedical applications of acoustically responsive phase shift nanodroplets: Current status and future directions," *Ultrason. Sonochemistry*, vol. 56, pp. 37–45, Sep. 2019.

[26] P. S. Sheeran et al., "Decafluorobutane as a phase-change contrast agent for low-energy extravascular ultrasonic imaging," *Ultrasound Med. Biol.*, vol. 37, no. 9, pp. 1518–1530, 2011.

[27] H. Yoon, K. A. Hallam, C. Yoon, and S. Y. Emelianov, "Super-resolution imaging with ultrafast ultrasound imaging of optically triggered perfluorohexane nanodroplets," *IEEE Trans. Ultrason., Ferroelectr., Freq. Control*, vol. 65, no. 12, pp. 2277–2285, Dec. 2018.

[28] G. Zhang et al., "Fast acoustic wave sparsely activated localization microscopy: Ultrasound super-resolution using plane-wave activation of nanodroplets," *IEEE Trans. Ultrason., Ferroelectr., Freq. Control*, vol. 66, no. 6, pp. 1039–1046, Jun. 2019.

[29] P. A. Mountford, W. S. Smith, and M. A. Borden, "Fluorocarbon nanodrops as acoustic temperature probes," *Langmuir*, vol. 31, no. 39, pp. 10656–10663, Oct. 2015.

[30] P. A. Mountford, S. R. Sirsi, and M. A. Borden, "Condensation phase diagrams for lipid-coated perfluorobutane microbubbles," *Langmuir*, vol. 30, no. 21, pp. 6209–6218, Jun. 2014.

[31] S. Lin et al., "Imaging of vaporised sub-micron phase change contrast agents with high frame rate ultrasound and optics," *Phys. Med. Biol.*, vol. 63, no. 6, Mar. 2018, Art. no. 065002.

[32] J. Yan, T. Zhang, J. Broughton-Venner, P. Huang, and M. X. Tang, "Super-resolution ultrasound through sparsity-based deconvolution and multi-feature tracking," *IEEE Trans. Med. Imag.*, vol. 41, no. 8, pp. 1938–1947, Aug. 2022.

[33] M. Krix, F. Kiessling, N. Farhan, K. Schmidt, J. Hoffend, and S. Delorme, "A multivessel model describing replenishment kinetics of ultrasound contrast agent for quantification of tissue perfusion," *Ultrasound Med. Biol.*, vol. 29, pp. 1421–1430, Oct. 2003.

[34] L. Wang and C. Mohan, "Contrast-enhanced ultrasound: A promising method for renal microvascular perfusion evaluation," *J. Transl. Internal Med.*, vol. 4, no. 3, pp. 104–108, Sep. 2016.

[35] H. Aldiwani, S. Mahdai, G. Alhatemi, and C. N. B. Merz, "Microvascular angina: Diagnosis and management," *Eur. Cardiol. Rev.*, vol. 16, p. e46, Dec. 2021.

[36] P. A. Mountford, A. N. Thomas, and M. A. Borden, "Thermal activation of superheated lipid-coated perfluorocarbon drops," *Langmuir*, vol. 31, no. 16, pp. 4627–4634, Apr. 2015.

[37] M. Seo, R. Williams, and N. Matsuura, "Size reduction of cosolvent-infused microbubbles to form acoustically responsive monodisperse perfluorocarbon nanodroplets," *Lab Chip*, vol. 15, no. 17, pp. 3581–3590, 2015.

[38] X. Zhou et al., "3D velocity and volume flow measurement *in vivo* using speckle decorrelation and 2D high frame rate contrast-enhanced ultrasound," *IEEE Trans. Ultrason., Ferroelectr., Freq. Control*, vol. 65, no. 12, pp. 1–11, Jun. 2018.

[39] S. K. Yarmoska, H. Yoon, and S. Y. Emelianov, "Lipid shell composition plays a critical role in the stable size reduction of perfluorocarbon nanodroplets," *Ultrasound Med. Biol.*, vol. 45, no. 6, pp. 1489–1499, Jun. 2019.

[40] T. M. Mitcham et al., "Effect of perfluorocarbon composition on activation of phase-changing ultrasound contrast agents," *Med Phys*, vol. 49, no. 4, pp. 2212–2219, Apr. 2022.

[41] P. S. Sheeran, S. H. Luois, L. B. Mullin, T. O. Matsunaga, and P. A. Dayton, "Design of ultrasonically-activatable nanoparticles using low boiling point perfluorocarbons," *Biomaterials*, vol. 33, pp. 3262–3269, Apr. 2012.

[42] F. Dong et al., "Blinking acoustic nanodroplets enable fast super-resolution ultrasound imaging," *ACS Nano*, vol. 15, no. 10, pp. 16913–16923, 2021.

[43] C.-H. Fan, Y.-T. Lin, Y.-J. Ho, and C.-K. Yeh, "Spatial-temporal cellular bioeffects from acoustic droplet vaporization," *Theranostics*, vol. 8, no. 20, pp. 5731–5743, 2018.

[44] D. L. Miller et al., "Bioeffects considerations for diagnostic ultrasound contrast agents," *J. Ultrasound Med.*, vol. 27, no. 4, pp. 611–632, 2008.

[45] M. Toulemonde, G. Zhang, R. J. Eckersley, and M.-X. Tang, "Flow visualization through locally activated nanodroplets and high frame rate imaging," in *Proc. IEEE Int. Ultrason. Symp. (IUS)*, Oct. 2018, pp. 1–4.

[46] O. Demeulenaere et al., "Coronary flow assessment using 3-dimensional ultrafast ultrasound localization microscopy," *Cardiovascular Imag.*, vol. 15, no. 7, pp. 1193–1208, Jul. 2022.

[47] P. Cormier, J. Poree, C. Bourquin, and J. Provost, "Dynamic myocardial ultrasound localization angiography," *IEEE Trans. Med. Imag.*, vol. 40, no. 12, pp. 3379–3388, Dec. 2021.

[48] S. Li, S. Lin, Y. Cheng, T. O. Matsunaga, R. J. Eckersley, and M.-X. Tang, "Quantifying activation of perfluorocarbon-based phase-change contrast agents using simultaneous acoustic and optical observation," *Ultrasound Med. Biol.*, vol. 41, no. 5, pp. 1422–1431, May 2015.

[49] C. Puett, P. S. Sheeran, J. D. Rojas, and P. A. Dayton, "Pulse sequences for uniform perfluorocarbon droplet vaporization and ultrasound imaging," *Ultrasonics*, vol. 54, no. 7, pp. 2024–2033, Sep. 2014.

[50] B. Jing, M. E. Brown, M. E. Davis, and B. D. Lindsey, "Imaging the activation of low-boiling-point phase-change contrast agents in the presence of tissue motion using ultrafast inter-frame activation ultrasound imaging," *Ultrasound Med. Biol.*, vol. 46, no. 6, pp. 1474–1489, Jun. 2020.

[51] K. P. Hadinger, J. P. Marshalek, P. S. Sheeran, P. A. Dayton, and T. O. Matsunaga, "Optimization of phase-change contrast agents for targeting MDA-MB-231 breast cancer cells," *Ultrasound Med. Biol.*, vol. 44, no. 12, pp. 2728–2738, Dec. 2018.

[52] A. Ishijima et al., "The lifetime evaluation of vapourised phase-change nano-droplets," *Ultrasonics*, vol. 69, pp. 97–105, Jul. 2016.

[53] Y. I. Zhu, H. Yoon, A. X. Zhao, and S. Y. Emelianov, "Leveraging the imaging transmit pulse to manipulate phase-change nanodroplets for contrast-enhanced ultrasound," *IEEE Trans. Ultrason., Ferroelectr., Freq. Control*, vol. 66, no. 4, pp. 692–700, Apr. 2018.

[54] N. Reznik et al., "The efficiency and stability of bubble formation by acoustic vaporization of submicron perfluorocarbon droplets," *Ultrasonics*, vol. 53, no. 7, pp. 1368–1376, Sep. 2013.

[55] M. T. Burgess, M. Aliabouzar, C. Aguilar, M. L. Fabiilli, and J. A. Ketterling, "Slow-flow ultrasound localization microscopy using recondensation of perfluoropentane nanodroplets," *Ultrasound Med. Biol.*, vol. 48, no. 5, pp. 743–759, May 2022.

[56] D. M. Brandner, X. Cai, J. Foiret, K. W. Ferrara, and B. G. Zagar, "Estimation of tissue attenuation from ultrasonic B-mode images—Spectral-log-difference and method-of-moments algorithms compared," *Sensors*, vol. 21, no. 7, p. 2548, Apr. 2021.

[57] T.-Y. Lai, M. Bruce, and M. A. Averkiou, "Modeling of the acoustic field produced by diagnostic ultrasound arrays in plane and diverging wave modes," *IEEE Trans. Ultrason., Ferroelectr., Freq. Control*, vol. 66, no. 7, pp. 1158–1169, Jul. 2019.